This article has been accepted for publication in IEEE Internet of Things Journal. This is the author's version which has not been fully edited and content may change prior to final publication. Citation information: DOI 10.1109/JIOT.2023.3245096

R-VLCP: Channel Modeling and Simulation in Retroreflective Visible Light Communication and Positioning Systems

Sihua Shao, *Member, IEEE*, Adrian Salustri, *Student Member, IEEE,* Abdallah Khreishah, *Senior Member, IEEE,* Chenren Xu, *Senior Member, IEEE, and Shuai Ma, Member, IEEE*

***Abstract*—Retroreflective visible light communication and positioning (R-VLCP) is a novel ultra-low-power Internet-of-Things (IoT) technology leveraging indoor light infrastructures. Compared to traditional VLCP, R-VLCP offers several additional favorable features including self-alignment, low-size, weight, and power (SWaP), glaring-free, and sniff-proof. In analogy to RFID, R-VLCP employs a microwatt optical modulator (e.g., LCD shutter) to manipulate the intensity of the reflected light from a corner-cube retroreflector (CCR) to the photodiodes (PDs) mounted on a light source. In our previous works, we derived a closed-form expression for the retroreflection channel model, assuming that the PD is much smaller than the CCR in geometric analysis. In this paper, we generalize the channel model to arbitrary size of PD and CCR. The received optical power is fully characterized relative to the sizes of PD and CCR, and the 3D location of CCR. We also develop a custom and open-source ray tracing simulator – RetroRay, and use it to validate the channel model. Performance evaluation of area spectral efficiency and horizontal location error is carried out based on the channel model validated by RetroRay. The results reveal that increasing the size of PD and the density of CCRs improves communication and positioning performance with diminishing returns.**

***Index Terms*—visible light communication, visible light positioning, backscatter communication, retroreflector, ultra-low-power, Internet-of-Things.**

I. Introduction

ONE of the top challenges of Internet-of-Things (IoT) communication and networking is the streamlined operations of vast connected endpoints, which demands extremely power-efficient connectivity for simple and quick device installation, alongside minimal battery replacement and recharging. For the seamless integration of new devices into IoT networks without disrupting the operations of existing devices, new wireless access medium, such as visible light spectrum, exhibits its unique value. Visible light communication (VLC) or LiFi infrastructural support is prospective: In June 2021 [1], global LiFi leader pureLiFi releases a video of the latest LiFi enabled phone, using two mobile phones with their Light Antenna technology . In December 2021 [2], pureLiFi has secured a multi-million dollar deal to supply the U.S. military with their Kitefin LiFi system. In February 2022 [3], pureLiFi demonstrates the first LiFi ecosystem for the home, which consists of a consumer style downlighter, a smartphone, a smart TV and an AR headset all connected by LiFi. The growing LiFi market is spurring the utilization of the unlicensed visible light spectrum in a low-size, weight, and power (SWaP) form.

Backscatter communication has been studied in radio frequency (RF) domain for decades, where RFID is one paradigm of backscattering the radio signals from a dedicated RF reader. Recent RF backscatter research efforts have focused on the exploitation of existing radio infrastructure (e.g., TV band [4], FM radio [5], WiFi [6]–[10] and LoRa [11], [12]). Instead of self-generating the RF signals, an RF backscatter harvests energy from the ambient signals and intelligently bounces the incident RF signals with modified amplitude/frequency/phase to the target receiver. RF backscatter demonstrates the potential to leverage RF wireless access infrastructure in a low-SWaP fashion. Nevertheless, the practical deployment of RF backscatter at scale faces several fundamental issues: interference to existing RF devices, wide interception range, low reuse factor, and low accuracy under non line-of-sight conditions.

To work around these issues, backscatter communication in optical domain, namely retroreflective VLC (RetroVLC) was first introduced in 2015 [13]. RetroVLC system leverages a retroreflector to return the incident light back to its source with minimum scattering. A retroreflector can be produced using a corner-cube with three mutually perpendicular reflective surfaces or sheeting like 3M Scotchlite reflective material fabrics [14]. Compared to the sheeting material, a corner-cube retroreflector (CCR) suffers less scattering effect and concentrates more reflected light back to the point where the light source locates at. To modulate the reflected optical signal, RetroVLC proposed to use a low-cost, low-SWaP, ultra-low-power and kHz-bandwidth optical modulator - LCD shutter [15]. An LCD shutter toggles the pass/block state by imposing an electric field on the liquid crystal layer. Retroreflective visible light communication and positioning (R-VLCP) extends the use of retroreflected uplink signal to positioning by analyzing the retroreflection path loss model [16]–[18]. Due to the retroreflection property, R-VLCP circumvents

S. Shao and A. Salustri are with the Department of Electrical Engineering, New Mexico Tech, Socorro, New Mexico, USA. E-mail: sihua.shao@nmt.edu, adrian.salustri@student.nmt.edu

A. Khreishah is with the Department of Electrical and Computer Engineering, New Jersey Institute of Technology, Newark, New Jersey, USA. E-mail: abdallah@njit.edu

X. Chenren is with the Department of Computer Science, Peking University, Beijing, China. E-mail: chenren@pku.edu.cn

M. Shuai is with the Peng Cheng Laboratory, Shenzhen, China. E-mail: mash01@pcl.ac.cn

Copyright (c) 2023 IEEE. Personal use of this material is permitted. However, permission to use this material for any other purposes must be obtained from the IEEE by sending a request to pubs-permissions@ieee.org.

Authorized licensed use limited to: UNIVERSITY OF NEW MEXICO. Downloaded on June 04,2023 at 15:25:36 UTC from IEEE Xplore. Restrictions apply.
© 2023 IEEE. Personal use is permitted, but republication/redistribution requires IEEE permission. See https://www.ieee.org/publications/rights/index.html for more information.

This article has been accepted for publication in IEEE Internet of Things Journal. This is the author's version which has not been fully edited and content may change prior to final publication. Citation information: DOI 10.1109/JIOT.2023.3245096

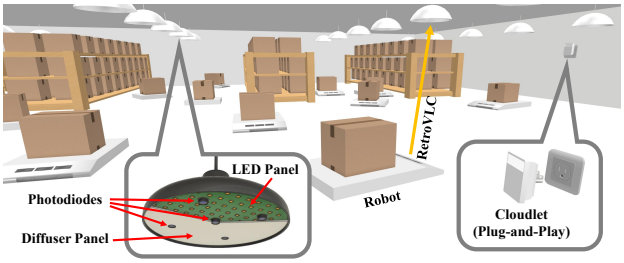

Fig. 1: A paradigm of R-VLCP in warehouse automation.

the uplink glaring effect and the strict alignment between two communication terminals, and also highly reduces the wireless interception range. Taking advantage of these unique features, R-VLCP can be applied in indoor wireless networks to secure the low-volume sensitive data exchange (e.g., key management) [19]. Exploiting the centimeter-level location error of R-VLCP, another promising application scenario, as shown in Fig. 1, is the multi-robot path planning in warehosue automation. The light infrastructure in a warehouse is utilized to track and control the sorting robots in real time, which can significantly improve the scalabiltiy compared to distributed heuristic solutions.

In some literature, RetroVLC is also referred to as visible light backscatter (VLB) due to its reflection-based signal generation mechanism. A pixelated VLB was prototyped in [20] to enable the multilevel backscattered signal. The authors of [21]–[23] proposed to encode data in mobile surfaces containing different reflecting materials. The work in [24] developed a trend-based modulation and code-assisted demodulation to boost the on-off keying-based VLB uplink data rate to 1 kbps. In [16]–[18], the retroreflection loss of a circular CCR was derived using geometric analysis. The work in [25] provided a comprehensive analysis of the physical layer design of VLB systems with a prototype using frequency shift keying. In [26], two polarizers of an LCD shutter was separated and a polarization-based differential reception was implemented to enable long-range VLB communication between a vehicle and road signs. The work in [27] developed a delayed superimposition modulation (DSM) to exploit the fast rising time of LCD shutter and integrate DSM with a polarization-based QAM by extending DSM symbols to the I-Q plane. The authors of [28] focused on the birefringence values and thicknesses of liquid crystal to improve the switching speed without significantly losing the contrast ratio. Most recently, another optical modulator called digital micro-mirror device was explored in [29] which trades off miliwatt power consumption for 10-fold data rate boosting.

To better understand the channel model of R-VLCP, in our previous works [16], [17], we derived a retroreflection path loss model for a circular CCR and validated the model by experiments. The derivation was inspired by the analysis of active reflecting area in [30]. The active reflecting area is an area of the front face of the CCR, which is characterized by the intersection of input aperture and output aperture, and any ray that is incident outside of the active reflecting area will not be retroreflected. In [16], [17], the analysis of active reflecting area was mapped onto the light source plane to delineate an effective reflecting area on the light source from which the rays are reflected back to the corresponding photodiode (PD) (Fig. 2) embedded on the light source. Our previous channel model [16], [17] was based on an assumption that the size of PD is much less than the size of CCR, and could generate inaccurate results otherwise. Although our previous works has shown that the retroreflection channel model can be accurately characterized using geometric analysis, *the assumption (PD $<<$ CCR) imposes severe limitations on the applicability of the channel model*. These limitations add barriers to hardware optimization of R-VLCP system designs. In this paper, we generalize the channel model to arbitrary size of PD and CCR, validate the channel model through ray tracing-based simulation, and evaluate the communication and positioning performance of R-VLCP systems based on the validated channel model. More specifically, our main contributions are summarized as follows:

- We parameterize (Sec. II) the CCR-based R-VLCP system and fully characterize (Sec. III) the area (A_{ERA}) of effective reflecting area (i.e., an area on the light source plane from which the emitted rays are reflected back to the PD sensing area) and the area (A_{PD}) of effective PD sensing area (i.e., entire or portion of the PD sensing area depending on the sizes of PD and CCR and the location of CCR) for arbitrary size of PD and CCR. The generalized retroreflection channel model is expressed in closed-form based on A_{ERA}, A_{PD}, and the free space optical path loss model.
- We develop RetroRay - a custom and open source ray tracing simulator (Sec. IV) to validate the closed-form expressions of A_{ERA} and A_{PD} derived in Sec. III using geometric analysis. Using RetroRay simulator, we run 10^8 rays for each location of CCR. The value of A_{ERA} is obtained by constructing the convex hull of the collection of effective starting points, from which the emitted rays are returned back to the PD sensing area. The value of A_{PD} is found by a two-part separation and delineating the non-convex boundary of each part. Extreme values of the sizes of PD and CCR and the height are tested. Mean theoretical error $< 1.2\%$ and maximum theoretical error $< 3\%$ are observed.
- Based on the generalized retroreflection channel model validated in Sec. IV, we conduct numerical analysis to evaluate the communication and positioning performance of R-VLCP systems (Sec. V). In particular, we compute the average area spectral efficiency (AASE) and the one-dimentional horizontal location error (e_{HLE}) in terms of different sizes of PD and different densities of CCRs. The numerical results reveal that as the size of PD or the density of CCRs increases, the improvement in AASE and e_{HLE} becomes less noticeable. The trade-offs imposed by increased modulation bandwidth, limited size of light source, and prism material are discussed further after the numerical analysis.

Authorized licensed use limited to: UNIVERSITY OF NEW MEXICO. Downloaded on June 04,2023 at 15:25:36 UTC from IEEE Xplore. Restrictions apply.
© 2023 IEEE. Personal use is permitted, but republication/redistribution requires IEEE permission. See https://www.ieee.org/publications/rights/index.html for more information.

This article has been accepted for publication in IEEE Internet of Things Journal. This is the author's version which has not been fully edited and content may change prior to final publication. Citation information: DOI 10.1109/JIOT.2023.3245096

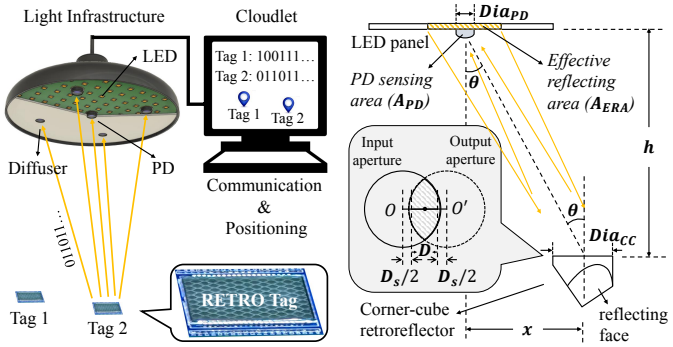

(a) system diagram (b) system parameters

Fig. 2: R-VLCP system diagram and system parameters.

II. Overview of the R-VLCP System

A. System Overview

The R-VLCP system diagram is depicted in Fig. 2a. Multiple PDs (i.e., anchors) are embedded into the LED panel to sense the reflected optical signal from RETRO tags. A diffuser layer is deployed on top of the LED panel to even out the light emission over the light emitting surface. In each RETRO tag, an LCD shutter is placed over a retroreflector (a single CCR or a CCR array) to modulate the reflected optical signal. The sensed signals of PDs are processed by a controller to demodulate and decode the data from each tag and to read the received signal strength (RSS) for positioning purpose. Due to the retro-reflection property, RETRO tags only reflect light back to its source. Therefore, the uplink interference among different tags can be modeled in the same way as the downlink VLC system [31]. Decomposition of communication and positioning signals has been studied in many literature [32]–[35], yet is out of the scope of this paper. As the location of a RETRO tag changes, so does the RSS read from all PDs, which is the result from the combination of free space optical path loss, effective reflecting area (A_{ERA}), and effective PD sensing area (A_{PD}).

B. System Parameters

To derive the closed-form expression of A_{ERA}, A_{PD} and also the received optical power, we define the following system parameters (notated in Fig. 2b):

1) The diameters of PD and CCR are denoted by Dia_{PD} and Dia_{CC}, respectively.
2) The PD is facing downward and the CCR is facing upward such that the radiance angle equals to the incidence angle and therefore are both notated by θ.
3) Due to isotropic nature of circular CCR, vertical distance h and horizontal distance x are sufficient to characterize the relative positions of PD and CCR.
4) The output aperture offsets D and D_s are determined by the length of CCR and the recessed length of CCR, respectively. The complete derivations of D and D_s are presented in ([30] Pages 10 and 14) and will be skipped in this paper.
5) For each PD, the transmitted optical power P_t is the total optical power emitted from the effective reflecting area (at $x = 0$) multiplied by the reflection loss. P_t can be accurately calibrated by several RSS measurements at different h with $x = 0$.
6) Lambertian index $ml = -\frac{\ln 2}{\ln(\cos \psi_{1/2})}$, where $\psi_{1/2}$ is the semi-angle at half power. $\psi_{1/2}$ can be measured by covering the light emitting surface with an opaque board while leaving a small hole in the middle.
7) Distance between PD and CCR $d = \sqrt{x^2 + h^2}$.

The parameters are summarized in Table I.

III. Analysis for the Received Optical Power

In this section, we derive the closed-form expressions of A_{ERA} and A_{PD} in terms of different Dia_{PD}, Dia_{CC}, and locations of the CCR. Upon those expressions, we further derive the received optical power using the free space optical path loss model [31].

TABLE I: Symbol Definition

Parameters	Definition
Dia_{CC}	Diameter of CCR
Dia_{PD}	Diameter of PD
A_{ERA}	Area of effective reflecting area
A_{PD}	Area of effective PD sensing area
θ	Radiance and incidence angles
D	Output aperture offset
D_s	Additional offset caused by recession
ml	Lambertian index
P_t	Transmitted optical power multiplied by reflector loss
h	Vertical distance between PD and CCR
x	Horizontal distance between PD and CCR
d	Distance between PD and CCR

A. Effective Reflecting Area

According to our previous works [16]–[18], the output aperture offset distance $\overline{OO'} = D + D_s$ (Fig. 2b), where D and D_s depend on the depth of CC and the recession length, respectively. The symmetry property of the incident ray (i.e., emitted from point P') and the retroreflected ray (i.e., falling on point P) has been utilized ([17], Fig. 5) to prove that the boundary of effective reflecting area is delineated by the trajectory of point P' (i.e., the starting point of a light ray that is ultimately captured by the PD sensing area) when rotating the intersection (i.e., elliptical leaf shape) of circle O and circle O' around point P (i.e., representing the location of PD). In this work, since the PD sensing area is generalized by a circle, point P becomes the intersection of the elliptical leaf and the PD sensing area (i.e., circle O_p in Fig. 3) when rotating the elliptical leaf around circle O_p and keeping them tangent to each other. Animation of delineating the boundary of effective reflecting area (i.e., the trajectory of P') is posted online[1]. In Theorem 1, we characterize A_{ERA} in terms of $D+D_s$, Dia_{CC} and Dia_{PD}, which can be further utilized in the free space optical path loss model.

Theorem 1. *Given the offset between the input aperture and the output aperture $D + D_s$, the diameter of CCR Dia_{CC}, the diameter of PD Dia_{PD}, the outer boundary of effective*

[1]YouTube URL: https://www.youtube.com/watch?v=i4athZiBkxo

Authorized licensed use limited to: UNIVERSITY OF NEW MEXICO. Downloaded on June 04,2023 at 15:25:36 UTC from IEEE Xplore. Restrictions apply.
© 2023 IEEE. Personal use is permitted, but republication/redistribution requires IEEE permission. See https://www.ieee.org/publications/rights/index.html for more information.

This article has been accepted for publication in IEEE Internet of Things Journal. This is the author's version which has not been fully edited and content may change prior to final publication. Citation information: DOI 10.1109/JIOT.2023.3245096

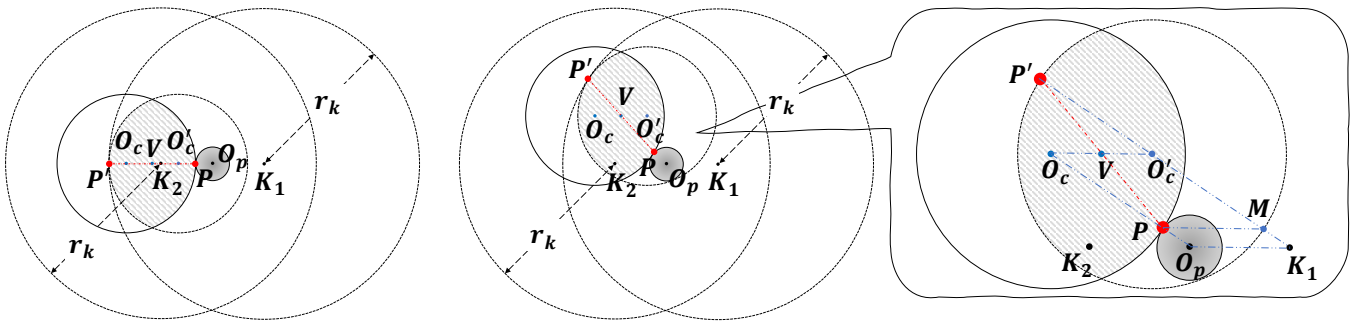

(a) $\angle P'K_1O_p$ equals to zero (b) $\angle P'K_1O_p$ equals to a non-zero value

Fig. 3: Four different cases when using the symmetry property of P' and P to analyze the boundary of effective reflecting area, which is the trajectory of P' when rotating P on circle O_p.

reflecting area is the outline of the intersection of two circles, of which the radii are $Dia_{CC} + Dia_{PD}/2$, and the distance is $2(D + D_s)$.

Proof. In Fig. 3, two large circles (K_1 and K_2), of which the radii are r_k (i.e., equal to $Dia_{CC} + Dia_{PD}/2$), are used to study the trajectory of P'. In Fig. 3a, $\angle P'K_1O_p = 0°$. Since $\overline{P'P} = Dia_{CC} - \overline{O_cO_c'}$, $\overline{PK_1} = r_k - \overline{P'P}$ and $\overline{O_pK_1} = \overline{O_cO_c'}$, $\overline{P'K_1} = r_k$ which indicates that P' is on circle K_1. In Figs. 3b, $\angle P'K_1O_p$ equals to a non-zero value. Assume line segment $\overline{P'K_1}$ intersects with circle O_c' at point M, since $\overline{O_cO_c'}$ is parallel to $\overline{O_pK_1}$ and $\overline{O_cP}$ is parallel to $\overline{O_c'M}$, the quadrilateral $O_cO_c'K_1O_p$ is a parallelogram, and we have $\overline{O_cP} = \overline{O_c'M} = Dia_{CC}/2$ and $\overline{MK_1} = \overline{PO_p} = Dia_{PD}/2$. Due to the symmetry property of P and P', we have $\overline{P'O_c'} = \overline{PO_c} = Dia_{CC}/2$. Therefore, $\overline{P'M} = \overline{P'O_c'} + \overline{O_c'M} + \overline{MK_1} = Dia_{CC} + Dia_{PD}/2 = r_K$. This indicates that P' is either on circle K_1 or on circle K_2 when we rotate the intersection of circles O_c and O_c' (i.e., the elliptical leaf region) around circle O_p and keep P as the tangent point of the elliptical leaf and circle O_p. Therefore, the boundary of effective reflecting area is the outline of the intersection of circles K_1 and K_2. □

In practice, the PD is mounted on top of the light emitting surface, and thereby no light ray is emitted from the PD sensing area. The area of effective reflecting area is characterized by the intersection of circles K_1 and K_2 subtracted by the PD sensing area,

$$A_{ERA} = 2r_k^2(\cos^{-1}\frac{D+D_s}{r_k} - \frac{D+D_s}{r_k}\sin(\cos^{-1}\frac{D+D_s}{r_k})) - \frac{1}{4}\pi Dia_{PD}^2.$$

A_{ERA} correction: In the effective reflecting area analysis, all the effective light rays (i.e., ultimately captured by the PD sensing area) are approximated to have the same radiance angle θ. The approximation incurs non-negligible error in the estimation of A_{ERA}, especially when x is close to zero. To complement the highly overestimated A_{ERA} at small value of x, the corrected horizontal distance x_c is given by

$$x_c = \max\{x, \frac{1}{2}(Dia_{PD} + Dia_{CC})\}.$$

B. Effective PD Sensing Area

In our previous works [16]–[18], we analyzed the case when $Dia_{CC} \gg Dia_{PD}$ such that the entire sensing area of the PD was fully utilized, and thereby the sensing area variable (i.e., A_{PD}) substituted in the free space optical path loss model [31] was simply the full area of the PD. Nevertheless, in this work, Dia_{CC} and Dia_{PD} are generalized to be any value. When $Dia_{CC} \ll Dia_{PD}$, the retroreflected light rays that are emitted from the boundary of the PD sensing area cannot reach back to the center of the PD sensing area. This leads to an unused area of the PD which depends on Dia_{CC}, Dia_{PD} and $D + D_s$. The effective PD sensing area (i.e., the area of the PD that captures retroreflected light rays) is the area of the PD minus the unused area.

The approach used to characterize the unused area of the PD is similar to the analysis of effective reflecting area. We rotate the intersection (or elliptical leaf) of circles O_c and O_c' inside circle O_p and keep P' as the tangent point of the elliptical leaf and circle O_p. Utilizing the symmetry property ([17], Fig. 5), the trajectory of P delineates the boundary of the unused area. As shown in Fig. 4c, when $\angle O_c'O_pR$ is relatively small, P is sliding on an arc. Once $\angle O_c'O_pR$ is sufficiently large such that P' reaches to the top of the elliptical leaf (Fig. 4a), P' will stay there as we rotate the elliptical leaf inside circle O_p. That means P starts sliding on another arc, of which the radius is $\frac{1}{2}Dia_{PD}$. Animation of delineating the boundary of effective PD sensing area (i.e., the trajectory of P) is posted online[2].

It can be observed from Fig. 4a that as Dia_{CC} increases, radius r_{sec} decreases, the blue sector region and the yellow trapezoid region reduces, and the upper and lower segments approach each other. The process is analogue to a closing eye. When Dia_{CC} increases up to $\frac{1}{2}Dia_{PD}$, $r_{sec} = 0$ and the eye completely closes. As shown in Fig. 5a, when $Dia_{CC} > \frac{1}{2}Dia_{PD}$, the distance l between P' and P determines $A_{segment}$. As l increases, $A_{segment}$ decreases. When l reaches up to $\frac{1}{2}Dia_{PD}$, $A_{segment} = 0$ and the entire PD sensing area is fully utilized. In Theorem 2, we characterize A_{PD} in terms of $D + D_s$, Dia_{CC} and Dia_{PD}, which can be further utilized in the free space optical path loss model.

[2]YouTube URL: https://www.youtube.com/watch?v=rpF1u_NPXhI

Authorized licensed use limited to: UNIVERSITY OF NEW MEXICO. Downloaded on June 04,2023 at 15:25:36 UTC from IEEE Xplore. Restrictions apply.
© 2023 IEEE. Personal use is permitted, but republication/redistribution requires IEEE permission. See https://www.ieee.org/publications/rights/index.html for more information.

This article has been accepted for publication in IEEE Internet of Things Journal. This is the author's version which has not been fully edited and content may change prior to final publication. Citation information: DOI 10.1109/JIOT.2023.3245096

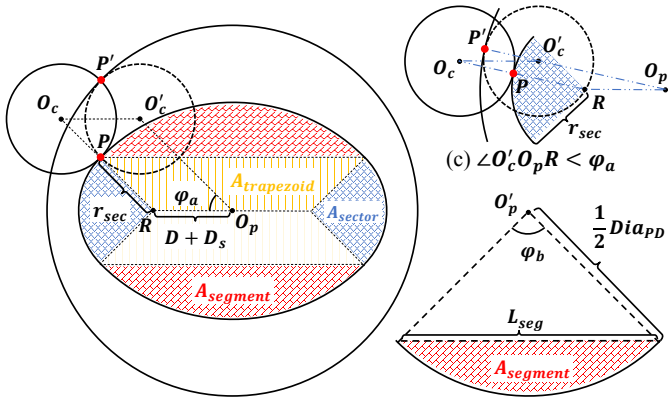

(a) A_{PD} analysis (case 1): trajectory of P (b) Area of segment

Fig. 4: Analysis of effective PD sensing area (case 1): when $Dia_{CC} < \frac{1}{2}Dia_{PD}$, the unused PD area consists of two sectors, two trapezoids and two segments.

Theorem 2. *Given the offset between the input aperture and the output aperture $D+D_s$, the diameter of CCR Dia_{CC}, the diameter of PD Dia_{PD}, the effective PD sensing area A_{PD} is characterized by three different cases as follows,*

1) *If $Dia_{CC} < \frac{1}{2}Dia_{PD}$, then*

$$A_{PD} = \frac{1}{4}\pi Dia_{PD}^2 - 2(A_{sector}+A_{trapezoid}+A_{segment}),$$

where

$$\begin{aligned} A_{sector} &= \varphi_a r_{sec}^2, \\ A_{trapezoid} &= \frac{1}{2} r_{sec}\sin\varphi_a\left[2(D+D_s)+L_{seg}\right], \\ A_{segment} &= \frac{1}{8}Dia_{PD}^2(\varphi_b - \sin\varphi_b), \end{aligned}$$

$$\begin{aligned} \varphi_a &= \arccos\left(\frac{D+D_s}{Dia_{CC}}\right), \\ r_{sec} &= \frac{1}{2}Dia_{PD} - Dia_{CC}, \\ L_{seg} &= 2(D+D_s) + 2r_{sec}\cos\varphi_a, \\ \varphi_b &= \arccos\left(1 - \frac{2L_{seg}^2}{Dia_{PD}^2}\right). \end{aligned}$$

2) *If $Dia_{CC} \geq \frac{1}{2}Dia_{PD}$ and $\sqrt{Dia_{CC}^2 - (D+D_s)^2} < \frac{1}{2}Dia_{PD}$, then*

$$A_{PD} = \frac{1}{4}\pi Dia_{PD}^2 - 2A_{segment},$$

where

$$\begin{aligned} A_{segment} &= \frac{1}{8}Dia_{PD}^2(\varphi_b - \sin\varphi_b), \\ \varphi_b &= 2\arccos\left(\frac{2\sqrt{Dia_{CC}^2 - (D+D_s)^2}}{Dia_{PD}}\right). \end{aligned}$$

3) *If $\sqrt{Dia_{CC}^2 - (D+D_s)^2} \geq \frac{1}{2}Dia_{PD}$, then*

$$A_{PD} = \frac{1}{4}\pi Dia_{PD}^2.$$

Proof. In case 1, as shown in Fig. 4 (c), since $\overline{O_cO'_c}$ is parallel to $\overline{RO_p}$ and $\overline{O_cR}$ is parallel to $P'O_p$, $r_{sec} = \overline{PR} = \frac{1}{2}Dia_{PD} - Dia_{CC}$. $\varphi_a = \angle PO_cO'_c = \arccos\frac{\frac{1}{2}\overline{O_cO'_c}}{\frac{1}{2}\overline{O_cP}} = \arccos\frac{D+D_s}{Dia_{CC}}$. L_{seg} is the lower base of the trapezoid and φ_b is calculated using the law of cosines. A_{sector}, $A_trapezoid$ and $A_{segment}$ can be found out using the area formula for each shape.

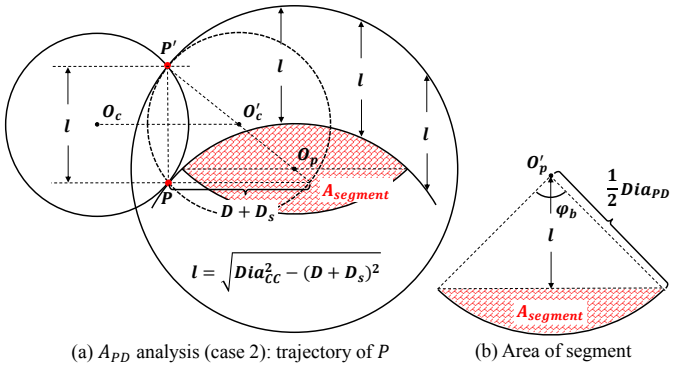

(a) A_{PD} analysis (case 2): trajectory of P (b) Area of segment

Fig. 5: Analysis of effective PD sensing area (case 2): when $Dia_{CC} \geq \frac{1}{2}Dia_{PD}$ and $\sqrt{Dia_{CC}^2 - (D+D_s)^2} < \frac{1}{2}Dia_{PD}$, the unused PD area consists of two segments.

In case 2, since the distance between P' and P is length $l = \sqrt{Dia_{CC}^2 - (D+D_s)^2}$, φ_b is calculated using the inverse of cosine function. The segment area formula can be used to find out $A_{segment}$.

As l increases in case 2, the unused PD area is gradually compressed. Therefore, in case 3, when $l \geq \frac{1}{2}Dia_{PD}$, the unused PD area reduces to zero, and A_{PD} is the full PD sensing area. □

C. Received Optical Power

Once we complete the characterization of A_{ERA}, a weighting factor ϵ is defined to describe the ratio of the current location-dependent A_{ERA} to the maximum A_{ERA}^{max} (i.e., $x = 0$ or $D + D_s = 0$), and

$$\epsilon = \frac{A_{ERA}}{A_{ERA}^{max}} = \frac{A_{ERA}}{\pi(r_k^2 - \frac{1}{4}Dia_{PD}^2)}.$$

Due to the property of retroreflection, the radiance angle from the effective reflecting area is equal to the incidence angle to the PD and the propagation distance is $2d$. According to the free space optical path loss model [31], the received optical power is

$$P_r = P_t \frac{(ml+1)A_{PD}}{8\pi d^2}\cos^{ml+1}\theta\epsilon. \tag{1}$$

Given Dia_{CC} and Dia_{PD}, the maximum A_{ERA} is deterministic, and thereby the value of P_t can be determined by an initial calibration, where n measurements of $\hat{P}_r$ are performed at different h with $x = 0$. The value of P_t is obtained by minimizing the mean square error $\frac{1}{n}\sum_{i=1}^{n}\left(P_r - \hat{P}_r\right)^2$.

IV. Ray Tracing-Based Simulation

A. Simulation Overview

Ray tracing-based simulations are used to validate the closed-form expressions for A_{ERA}, ϵ, and A_{PD} derived in

Authorized licensed use limited to: UNIVERSITY OF NEW MEXICO. Downloaded on June 04,2023 at 15:25:36 UTC from IEEE Xplore. Restrictions apply.
© 2023 IEEE. Personal use is permitted, but republication/redistribution requires IEEE permission. See https://www.ieee.org/publications/rights/index.html for more information.

This article has been accepted for publication in IEEE Internet of Things Journal. This is the author's version which has not been fully edited and content may change prior to final publication. Citation information: DOI 10.1109/JIOT.2023.3245096

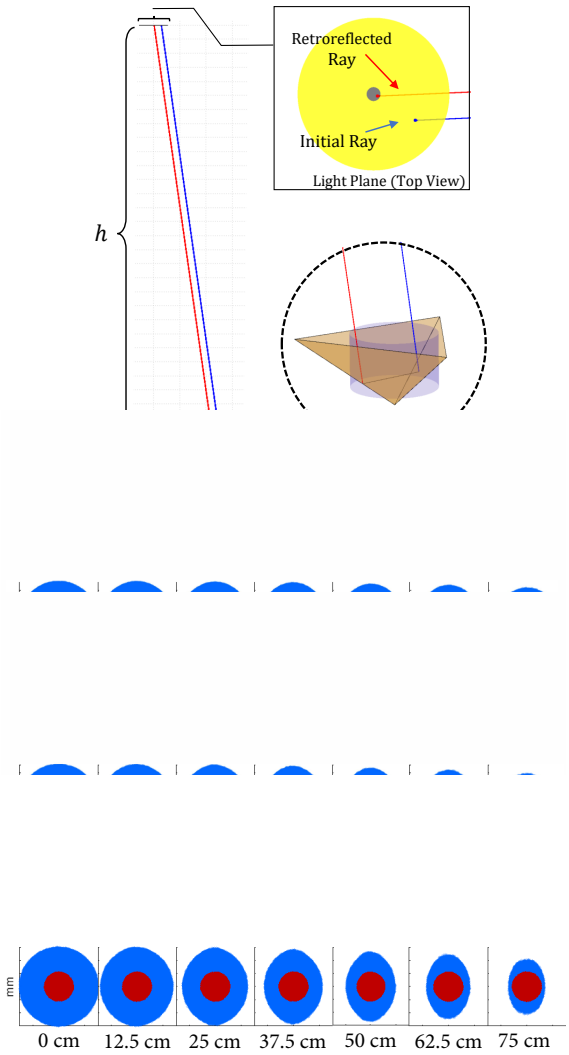

(c) $Dia_{PD} = 10$ mm, $Dia_{CC} = 10$ mm

Fig. 7: Visualization of effective reflecting area (blue region) and effective PD sensing area (red region) as x increases from 0 to 75 cm.

Section III. The areas A_{ERA} and A_{PD} are determined by recording the initial and final locations of retroreflected rays, and identifying the boundaries of the the regions of interest. Simulation results agree well with theoretical results for a wide range of input parameter values (i.e., Dia_{PD}, Dia_{CC} and h). We conclude that the derived channel model (Eq. 1) is accurate and can be used for further analysis of R-VLCP performance.

B. Ray Generation and Ray Detection

To gain the complete control over ray generation and ray detection (and cultivate future R-VLCP research), we develop RetroRay, a ray tracing package written in MATLAB [36]. RetroRay is a parallel ray tracer, meaning the distance to all objects are calculated at once and the closest one is chosen as the real collision. The simulation continues until the ray hits an absorber, a detector, or nothing. Scenes are constructed from optical primitives, such as a triangle, a circle, a circular aperture, and a cylindrical tube. Each primitive can be configured as a reflector, an absorber or a detector.

TABLE II: Parameters for evaluating A_{ERA} and ϵ

	Dia_{PD} (mm)	Dia_{CC} (mm)	h(m)
Trial 1	0.1, 1, 10	10	1.5
Trial 2	10	1, 10, 50	1.5
Trial 3	1	50	1.5, 3.0, 4.5

TABLE III: Parameters for evaluating A_{PD}

	Dia_{PD} (mm)	Dia_{CC} (mm)	h(m)
Trial 1	1, 2, 5	1	1.5
Trial 2	10	1, 5, 10	1.5
Trial 3	10	5	1.5, 3, 4.5

As shown in Fig. 6, three triangular reflectors are arranged to form the CCR's perpendicular faces. The front face of CCR is a circular aperture, and the recession is implemented by a cylindrical tube. A circular PD is embedded in the light plane which is h meters above the horizontal plane where the CCR moves. The light emitting surface of the light source is represented by the yellow circle, of which the diameter is heuristically set to $Dia_{PD} + 2Dia_{CC}$. An initial ray always starts from a point in the yellow circle. The diameters of the CCR and the PD are varying and summarized in Table II and Table III.

The simulation starts with Monte Carlo ray generation, where points are randomly sampled with a uniform distribution from the light source plane and the CCR's front face. The ray connecting the two points (one from the light source plane and the other one from the CCR's front face) is used to represent an incident ray to the front face of CCR. This method is chosen for the sake of computational efficiency, since it guarantees that every incident ray will hit the CCR's front face.

If the retroreflected ray hits the PD sensing area, the ray path is logged for later analysis. The final output is a tuple (P_0, P_f) for every detected ray, where $P_0 = (x_0, y_0, 0)$ is the starting position of the randomly generated initial ray, and $P_f = (x_f, y_f, h)$ is the detected position of the retroreflected ray on the PD sensing area. Fig. 6 shows one example of ray trace with P_0 colored blue and P_f colored red. To better understand the variation of A_{ERA} and A_{PD}, exemplary collections of tuple (P_0, P_f) are plotted in Fig. 7 to visualize the change of A_{ERA} and A_{PD} as x increases. In Fig. 7, $h = 1.5$ m, and three candidate sets of (Dia_{PD}, Dia_{CC}) are selected to reveal the three different cases of A_{PD} progression.

C. Validation Methodology

Two simulations ($Sim1$ and $Sim2$) are performed to quantitatively study the theoretical errors for A_{ERA}, ϵ, and A_{PD}. $Sim1$ aims at evaluating A_{ERA} and ϵ. The parameters of $Sim1$ are listed in Table II and the results are presented in Figs. 8 and 9. The parameters are chosen to demonstrate a wide range of practical device sizes and locations. $Sim2$ aims at evaluating A_{PD}. The parameters of $Sim2$ are shown in Table III and results are plotted in Fig. 10. The selected parameters cover all the three cases in the A_{PD} derivation, which is realized by varying the ratio between Dia_{PD} and Dia_{CC}. In each trial of $Sim1$ and $Sim2$, for the three variables Dia_{PD}, Dia_{CC} and h, we simulate three different values of one variable while holding the others constant. Each trial

Authorized licensed use limited to: UNIVERSITY OF NEW MEXICO. Downloaded on June 04,2023 at 15:25:36 UTC from IEEE Xplore. Restrictions apply.
© 2023 IEEE. Personal use is permitted, but republication/redistribution requires IEEE permission. See https://www.ieee.org/publications/rights/index.html for more information.

This article has been accepted for publication in IEEE Internet of Things Journal. This is the author's version which has not been fully edited and content may change prior to final publication. Citation information: DOI 10.1109/JIOT.2023.3245096

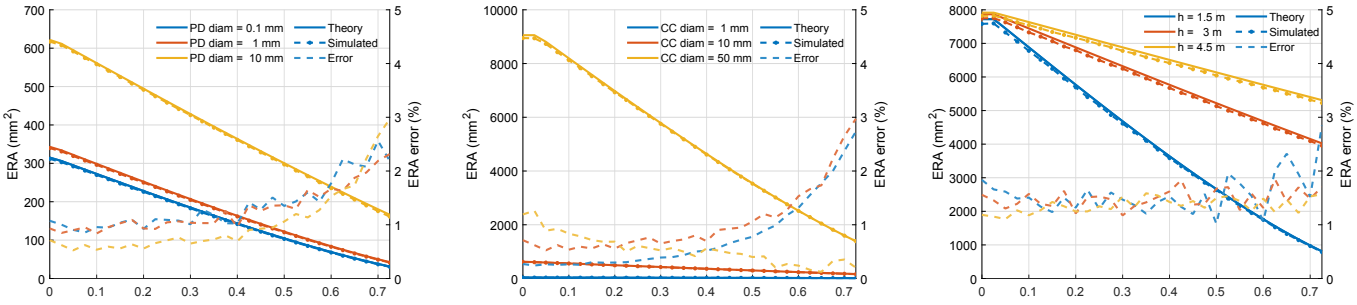

(a) A_{ERA} Trial 1 (variable Dia_{PD}) (b) A_{ERA} Trial 2 (variable Dia_{CC}) (c) A_{ERA} Trial 3 (variable h)

Fig. 8: Simulated and theoretical A_{ERA} values using parameters in Table II. (Mean error $= 1.16\%$, Max error $= 2.97\%$)

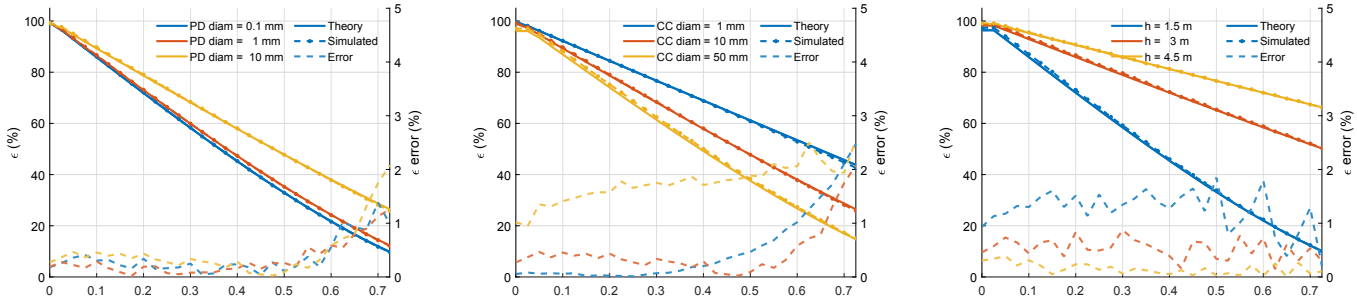

(a) ϵ Trial 1 (variable Dia_{PD}) (b) ϵ Trial 2 (variable Dia_{CC}) (c) ϵ Trial 3 (variable h)

Fig. 9: Simulated and theoretical ϵ values using parameters in Table II. (Mean error $= 0.64\%$, Max error $= 2.54\%$)

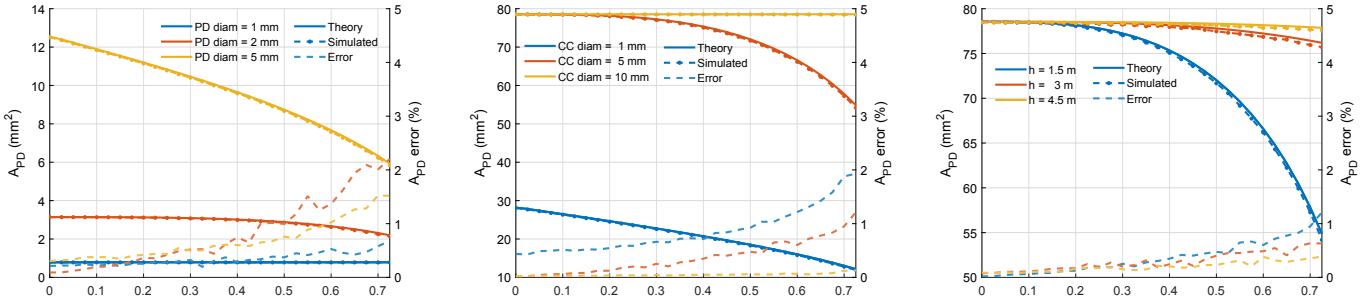

(a) A_{PD} Trial 1 (variable Dia_{PD}) (b) A_{PD} Trial 2 (variable Dia_{CC}) (c) A_{PD} Trial 3 (variable h)

Fig. 10: Simulated and theoretical A_{PD} values using parameters in Table III. (Mean error $= 0.44\%$, Max error $= 2.20\%$)

uses 10^8 rays at 30 different values of x. The methods for quantifying A_{ERA}, ϵ, and A_{PD} are elaborated below.

1) A_{ERA}: The effective reflecting area (visualized as the blue region in Fig. 7) is the area enclosing the initial positions of all detected rays on the light plane. The effective reflecting area is found by constructing the convex hull of the collection of P_0, integrating around its boundary, and subtracting the PD sensing area.

2) ϵ: After determining the A_{ERA} for all values of x, ϵ is calculated by normalizing by A_{ERA}^{max} (i.e., obtained at $x = 0$).

3) A_{PD}: Effective PD sensing area (visualized as the red region in Fig. 7) is the area enclosing the final positions of all detected rays on the PD surface. As discussed in Sec. III-B, when $Dia_{CC} << Dia_{PD}$, the detected rays will not cover all of the PD sensing area, so $A_{PD} \neq \frac{1}{4}\pi(Dia_{PD})^2$ in general. Therefore, we need to quantify the A_{PD} in a similar way to quantifying A_{ERA}. The geometry of A_{PD} may have a hole in the center which makes the convex hull method inaccurate. To resolve this, we divide the A_{PD} region into two parts and then use MATLAB's boundary function to generate non-convex boundaries. Finally, the two boundary loops are integrated and added together.

D. Discussion of Results and Error

The simulated results of A_{ERA}, ϵ, and A_{PD} are compared against the theoretical values derived in Sec. III. Figs. 8 and 9 plot the values of A_{ERA} and ϵ for each trial in $Sim1$. Fig. 10 plots the value of A_{PD} for each trial in $Sim2$. The x-axis represents the horizontal position of the CCR with respect to the origin ($x = 0$). The solid and dot-dashed lines show the theoretical and simulation results, respectively, and are plotted against the left y-axis. The dashed lines show the percentage error between the two, and are plotted against the right y-axis.

Authorized licensed use limited to: UNIVERSITY OF NEW MEXICO. Downloaded on June 04,2023 at 15:25:36 UTC from IEEE Xplore. Restrictions apply.
© 2023 IEEE. Personal use is permitted, but republication/redistribution requires IEEE permission. See https://www.ieee.org/publications/rights/index.html for more information.

This article has been accepted for publication in IEEE Internet of Things Journal. This is the author's version which has not been fully edited and content may change prior to final publication. Citation information: DOI 10.1109/JIOT.2023.3245096

Overall, the theoretical values match closely with the simulated values. The mean errors are under 1.2% and max errors are under 3% in all cases. One of the causes of the theoretical error is the method used to determine the effective reflecting area and effective PD sensing area. RetroRay returns a point cloud of detected rays and we construct the boundary numerically as described in Sec. IV-C. Since the points will never completely fill the regions of interest, the quantified area will always be slightly less than the ground truth. In Figs. 8 and 10, the simulated A_{ERA} and A_{PD} are hence strictly smaller than the theoretical values in all cases. At large x, the effective reflecting area and effective PD sensing area become very small such that the total number of detected rays will drop. The reduction in the number of points in the cloud leads to an increase in error due to the way the boundaries are drawn. In fact, as we increase the number of generated rays during the simulation, it can be observed that the error decreases significantly. From this, we conclude that the theoretical derivation is accurate and can be used for further analysis of the R-VLCP performance.

V. Performance Evaluation of R-VLCP

In this section, Dia_{CC} and Dia_{PD} are considered as variables to evaluate their impacts on the communication and positioning performance of R-VLCP systems. Therefore, we need to multiply P_t by a scaling factor δ to incorporate the change of the maximum A_{ERA}^{max}. In particular, for a specific pair of $Dia_{CC} = Dia_1$ and $Dia_{PD} = Dia_2$, we can find out the corresponding $A_{ERA}^{max} = E_1$ and determine the value of P_t through an initial calibration. When we change the values of Dia_{CC} and Dia_{PD}, $\delta = \frac{A_{ERA}^{max}}{E_1}$. Accordingly,

$$P_r = P_t \delta \frac{(ml+1)A_{PD}}{8\pi d^2} \cos^{ml+1}\theta\epsilon. \tag{2}$$

In our previous works [16], [17], the selected pair of Dia_{CC} and Dia_{PD} are $Dia_1 = 50$ mm and $Dia_2 = 13.82$ mm, respectively. Therefore, $E_1 = \pi[(Dia_1 + Dia_2/2)^2 - \frac{1}{4}Dia_2^2] \approx 10^4$ mm^2. Based on the experimental validation in our previous works [16], [17], the estimated value of P_t is 0.33 W. In the following, we use $E_1 = 10^4$ mm^2 and $P_t = 0.33$ W to evaluate the performance of R-VLCP systems. Note that the estimation error of P_t does not affect the optimization of Dia_{CC} and Dia_{PD}.

A. Communication

The main noise factors at the optical receiver are shot noise and thermal noise [31], [37], [38]. At low bandwidth, shot noise dominates thermal noise.

$$\sigma_{shot}^2 = 2q\gamma P_n B \quad \text{A}^2/\text{Hz},$$

where q is electron charge, γ is the average responsivity of the photodiode over the used wavelength band given in A/W, P_n is the average optical power of the received signal and the background illumination, and B is the equivalent noise bandwidth. In R-VLCP systems, the bandwidth of the state-of-the-art optical modulator is only up to kHz level, and thereby the thermal noise $\sigma_{thermal}^2$ can be neglected. In addition, since the background illumination in R-VLCP systems is much stronger than the received optical power from the RETRO tag, we can approximate P_n as a constant.

The signal to noise ratio (SNR) is expressed as

$$\text{SNR} = \frac{(\gamma P_r)^2}{\sigma_{shot}^2},$$

where P_r is calculated by Eq. 2. Using Shannon–Hartley theorem, the maximum spectral efficiency (SE) is

$$\text{SE} = \log_2(1 + \text{SNR}) \quad \text{bit/s/Hz}.$$

Since the user devices under a single R-VLCP access point (AP) share the same bandwidth B, the average area spectral efficiency (AASE) can be estimated by

$$\text{AASE} = \frac{\frac{1}{N_u}\sum_{k=1}^{N_u} \text{SE}_k}{\pi R_c^2} \quad \text{bit/s/Hz/m}^2,$$

where N_u is the number of candidate locations of the RETRO tag and R_c is the radius of AP coverage area.

TABLE IV: Parameters for AASE and e_{HLE} Analysis

Symbol	Value	Symbol	Value	Symbol	Value
P_t	0.33 W	Dia_1	50 mm	Dia_2	13.82 mm
h	1.5 m	ml	1	γ	0.25 A/W
P_n	0.02 W	B	5 kHz	R_c	0.8 m

To evaluate the AASE under different settings of Dia_{PD} and Dia_{CC}, we perform numerical analysis using the parameters listed in Table IV. We generate 10^6 random RETRO tag locations with uniform distribution inside the AP coverage area, In practical deployment, the size of RETRO tag is typically confined. Therefore, we limit the CCR array size to a 50 mm x 50 mm area and vary the number of CCRs using a grid structure. For instance, if the number of CCRs in one row/column is 5, then Dia_{CC} of each CCR is 50 mm/5 = 10 mm. As shown in Fig. 11, as the number of CCRs increases, AASE converges to different values for different sizes of PD. The diminishing return in AASE is caused by the under-utilization of the PD sensing area, which occurs at small Dia_{CC}. The results also indicate that increasing the size of PD will end up with a better AASE.

B. Positioning

Multiple PDs mounted on a single light source are utilized as anchors to localize the RETRO tag. Conceptually, PDs that are close together cannot provide as much information as PDs that are widely separated. Here, rather than studying different topologies of PDs, we mainly focus on the impact of Dia_{CC} and Dia_{PD} on the one-dimensional dilution of precision, namely horizontal location error (HLE) $e_{HLE} = |\hat{x} - x|$, where $\hat{x}$ is the measured horizontal distance.

To evaluate e_{HLE} under different settings of Dia_{PD} and Dia_{CC}, we perform numerical analysis using the parameters listed in Table IV. Here the equivalent noise bandwidth B is the same as the communication setting since the R-VLCP system is typically used for joint communication and positioning. We generate 10^5 different values of x uniformly in the range of $[0, R_c]$. For each value of x, P_r is calculated by Eq. 2, and

Authorized licensed use limited to: UNIVERSITY OF NEW MEXICO. Downloaded on June 04,2023 at 15:25:36 UTC from IEEE Xplore. Restrictions apply.
© 2023 IEEE. Personal use is permitted, but republication/redistribution requires IEEE permission. See https://www.ieee.org/publications/rights/index.html for more information.

This article has been accepted for publication in IEEE Internet of Things Journal. This is the author's version which has not been fully edited and content may change prior to final publication. Citation information: DOI 10.1109/JIOT.2023.3245096

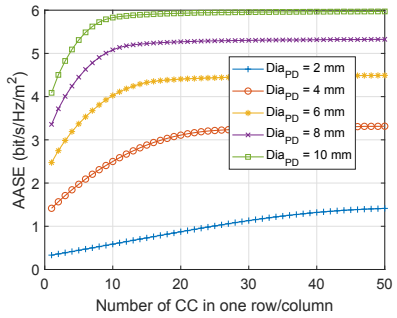

Fig. 11: AASE vs. density of CCRs for different sizes of PD

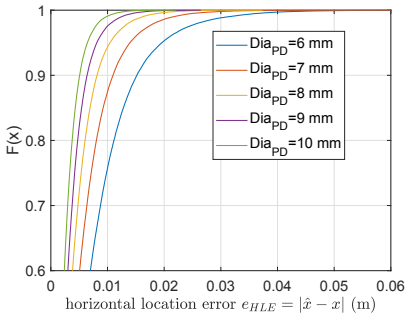

Fig. 12: Empirical CDF of e_{HLE} for different sizes of PD

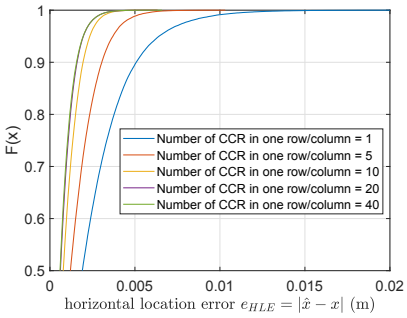

Fig. 13: Empirical CDF of e_{HLE} for different sizes of CCR

the measured received optical power $\hat{P}_r = P_r + N_0$, where $N_0 \sim \mathcal{N}(0, \sigma^2_{shot})$. Lastly, $\hat{x}$ is obtained using the Dichotomy method. In Fig. 12, $Dia_{CC} = 50$ mm, the CDF of e_{HLE} is evaluated for five different values of Dia_{PD}. The centimeter level location error is consistent with the experimental results in our previous works [16], [17]. As Dia_{PD} increases, the location accuracy improves due to higher SNR. In Fig. 13, $Dia_{PD} = 10$ mm, and similar to the AASE analysis, we limit the CCR array size to a 50 mm x 50 mm area and vary the number of CCRs using a grid structure. The location accuracy does not improve further once the number of CCR in one row/column reaches 20. The results are consistent with the AASE performance presented in Fig. 11.

C. Discussion

MHz-level optical modulator: The return of increasing Dia_{PD} is diminishing for both communication and positioning performance of R-VLCP systems. As the technologies of optical shutters advance, increasing Dia_{PD} may trade off the SNR, once the 3 dB bandwidth of the optical modulator is able to reach MHz level. This is because a larger PD provides higher response time or lower bandwidth [39]. An optimal value of Dia_{PD} shall be observed when seeking to maximize the SNR at high frequency band.

Limited size of light source: In practice, the area of the light emitting surface is confined. The light source design shown in Fig. 2a indicates that the actual area of the light emitting surface is the total area minus the area occupied by the PDs. A dense deployment of PDs may improve the uplink communication performance, while once the effective reflecting area starts overlapping with each other the distinguishability among different anchors (i.e., embedded PDs) will be poor, and thereby worse positioning accuracy. Such eclipsing effect will be more severe when Dia_{CC} is large. Intuitively, the optimal structure of the light AP is to wrap the LED chips around each PD, which results in another trade-off between manufacturing cost and system performance.

Prism material: High reuse factor is one of the major advantages of the optical backscatter when compared to the RF backscatter. For a hollow CCR, when $h = 1.5$ m, A_{ERA} approaches to 0 at $x = 0.9$ m. In other words, the radius of the coverage area of one light AP is around 0.9 m with 1.5 m height. One approach to expand the coverage area is to fill the CCR with prism material, such as N-BK7 [40]. The prism material has a refractive index $\eta > 1$ such that the declining speed of A_{ERA} slows down as x increases. Although a larger value of η leads to higher SNR, it does not change the maximum SNR at $x = 0$, which means that the distinguishability along the x axis is getting worse and thereby lower location accuracy.

Arbitrary orientation of RETRO tag: The case of arbitrary elevation and azimuth angles of RETRO tag has been studied in our previous work (Section 3.3 in [17]) and the analysis indicates that the elliptical region becomes the intersection of two ovals instead of two circles. A_{ERA} and A_{PD} can be determined by rotating the elliptical intersection externally and internally around circle O_p and delineate the trajectory of P' and P, respectively. Due to the extensive geometric derivation needed for the irregular shapes, it would be more efficient to compute A_{ERA} and A_{PD} using interactive geometry software.

VI. Conclusion

R-VLCP is a promising VLC-based technology to resolve the top challenges of IoT communication and networking, thanks to its unique features, such as self-alignment, glaring-free, sniff-proof, low-SWaP, high SNR and high reuse factor. In this paper, we fully characterize the path loss model of R-VLCP using the CCR - a type of retroreflector with the lowest reflection loss. A closed-form expression for received optical power is derived through geometric analysis and validated by our developed RetroRay - a custom and open source ray tracing-based simulator. The analytical model enables the quick computation of SNR for dynamic Dia_{PD}, Dia_{CC} and locations of PD and CCR. Analytical results are used to evaluate the performance of communication and positioning, which has revealed that increasing the size of PD and the density of CCRs enhances AASE and e_{HLE} but with diminishing returns. Consider a defined environment (e.g., warehouse) with standardized illumination requirements, the optimal size of PD and CCRs can be empirically determined with low computational complexity. The shadow effect and line-of-sight blockage of RETRO tag will be investigated in future work.

Acknowledgments

This work was supported by NSF grant OIA-1757207.

Authorized licensed use limited to: UNIVERSITY OF NEW MEXICO. Downloaded on June 04,2023 at 15:25:36 UTC from IEEE Xplore. Restrictions apply.
© 2023 IEEE. Personal use is permitted, but republication/redistribution requires IEEE permission. See https://www.ieee.org/publications/rights/index.html for more information.

This article has been accepted for publication in IEEE Internet of Things Journal. This is the author's version which has not been fully edited and content may change prior to final publication. Citation information: DOI 10.1109/JIOT.2023.3245096

REFERENCES

[1] pureLiFi, https://purelifi.com/lifi-enabled-phone/, 2021, [Online].

[2] ——, https://purelifi.com/us-army-expand-lifi-deployment/, 2021, [Online].

[3] ——, https://purelifi.com/purelifi-pushes-connectivity-in-the-home-to-new-limits-with-lifihome/, 2022, [Online].

[4] V. Liu, A. Parks, V. Talla, S. Gollakota, D. Wetherall, and J. R. Smith, "Ambient backscatter: Wireless communication out of thin air," *ACM SIGCOMM computer communication review*, vol. 43, no. 4, pp. 39–50, 2013.

[5] A. Wang, V. Iyer, V. Talla, J. R. Smith, and S. Gollakota, "FM backscatter: Enabling connected cities and smart fabrics," in *14th USENIX Symposium on Networked Systems Design and Implementation (NSDI 17)*, 2017, pp. 243–258.

[6] B. Kellogg, A. Parks, S. Gollakota, J. R. Smith, and D. Wetherall, "Wi-Fi backscatter: Internet connectivity for RF-powered devices," in *Proceedings of the 2014 ACM Conference on SIGCOMM*, 2014, pp. 607–618.

[7] D. Bharadia, K. R. Joshi, M. Kotaru, and S. Katti, "Backfi: High throughput wifi backscatter," *ACM SIGCOMM Computer Communication Review*, vol. 45, no. 4, pp. 283–296, 2015.

[8] B. Kellogg, V. Talla, S. Gollakota, and J. R. Smith, "Passive Wi-Fi: Bringing low power to Wi-Fi transmissions," in *13th USENIX Symposium on Networked Systems Design and Implementation (NSDI 16)*, 2016, pp. 151–164.

[9] P. Zhang, D. Bharadia, K. Joshi, and S. Katti, "Hitchhike: Practical backscatter using commodity wifi," in *Proceedings of the 14th ACM Conference on Embedded Network Sensor Systems CD-ROM*, 2016, pp. 259–271.

[10] R. Zhao, F. Zhu, Y. Feng, S. Peng, X. Tian, H. Yu, and X. Wang, "Ofdma-enabled wi-fi backscatter," in *The 25th Annual International Conference on Mobile Computing and Networking*, 2019, pp. 1–15.

[11] V. Talla, M. Hessar, B. Kellogg, A. Najafi, J. R. Smith, and S. Gollakota, "Lora backscatter: Enabling the vision of ubiquitous connectivity," *Proceedings of the ACM on interactive, mobile, wearable and ubiquitous technologies*, vol. 1, no. 3, pp. 1–24, 2017.

[12] Y. Peng, L. Shangguan, Y. Hu, Y. Qian, X. Lin, X. Chen, D. Fang, and K. Jamieson, "Plora: A passive long-range data network from ambient lora transmissions," in *Proceedings of the 2018 conference of the ACM special interest group on data communication*, 2018, pp. 147–160.

[13] J. Li, A. Liu, G. Shen, L. Li, C. Sun, and F. Zhao, "Retro-vlc: Enabling battery-free duplex visible light communication for mobile and iot applications," in *Proceedings of the 16th International Workshop on Mobile Computing Systems and Applications*, 2015, pp. 21–26.

[14] 3M, https://www.3m.com/3M/en_US/p/c/ppe/apparel/reflective-fabrics/i/safety/personal-safety/, [Online].

[15] Liquid Crystal Technologies, http://www.liquidcrystaltechnologies.com/, [Online].

[16] S. Shao, A. Khreishah, and I. Khalil, "Retro: Retroreflector based visible light indoor localization for real-time tracking of iot devices," in *IEEE INFOCOM 2018-IEEE Conference on Computer Communications*. IEEE, 2018, pp. 1025–1033.

[17] ——, "Enabling real-time indoor tracking of iot devices through visible light retroreflection," *IEEE Transactions on Mobile Computing*, vol. 19, no. 4, pp. 836–851, 2019.

[18] S. Shao, A. Khreishah, and J. Paez, "Passiveretro: Enabling completely passive visible light localization for iot applications," in *IEEE INFOCOM 2019-IEEE Conference on Computer Communications*. IEEE, 2019, pp. 1540–1548.

[19] NM EPSCoR, https://www.nmepscor.org/events/visible-light-communication-and-applications-smart-grids, [Online].

[20] S. Shao, A. Khreishah, and H. Elgala, "Pixelated VLC-backscattering for self-charging indoor IoT devices," *IEEE Photonics Technology Letters*, vol. 29, no. 2, pp. 177–180, 2016.

[21] Q. Wang, M. Zuniga, and D. Giustiniano, "Passive communication with ambient light," in *Proceedings of the 12th International on Conference on emerging Networking EXperiments and Technologies*, 2016, pp. 97–104.

[22] R. Bloom, M. Zuniga, Q. Wang, and D. Giustiniano, "Tweeting with sunlight: Encoding data on mobile objects," in *IEEE INFOCOM 2019-IEEE Conference on Computer Communications*. IEEE, 2019, pp. 1324–1332.

[23] W. Wang, Q. Wang, J. Zhang, and M. Zuniga, "Passivevlp: Leveraging smart lights for passive positioning," *ACM Transactions on Internet of Things*, vol. 1, no. 1, pp. 1–24, 2020.

[24] X. Xu, Y. Shen, J. Yang, C. Xu, G. Shen, G. Chen, and Y. Ni, "PassiveVLC: Enabling practical visible light backscatter communication for battery-free IoT applications," in *Proceedings of the 23rd Annual International Conference on Mobile Computing and Networking*, 2017, pp. 180–192.

[25] R. Bloom, M. Z. Zamalloa, and C. Pai, "Luxlink: creating a wireless link from ambient light," in *Proceedings of the 17th Conference on Embedded Networked Sensor Systems*, 2019, pp. 166–178.

[26] P. Wang, L. Feng, G. Chen, C. Xu, Y. Wu, K. Xu, G. Shen, K. Du, G. Huang, and X. Liu, "Renovating road signs for infrastructure-to-vehicle networking: a visible light backscatter communication and networking approach," in *Proceedings of the 26th Annual International Conference on Mobile Computing and Networking*, 2020, pp. 1–13.

[27] Y. Wu, P. Wang, K. Xu, L. Feng, and C. Xu, "Turboboosting visible light backscatter communication," in *Proceedings of the Annual conference of the ACM Special Interest Group on Data Communication on the applications, technologies, architectures, and protocols for computer communication*, 2020, pp. 186–197.

[28] S. K. Ghiasi, M. A. Z. Zamalloa, and K. Langendoen, "A principled design for passive light communication," in *Proceedings of the 27th Annual International Conference on Mobile Computing and Networking*, 2021, pp. 121–133.

[29] T. Xu, M. C. Tapia, and M. Zúñiga, "Exploiting digital Micro-Mirror devices for ambient light communication," in *19th USENIX Symposium on Networked Systems Design and Implementation (NSDI 22)*, 2022, pp. 387–400.

[30] D. A. Arnold, "Method of calculating retroreflector-array transfer functions," *SAO Special Report*, vol. 382, 1979.

[31] T. Komine and M. Nakagawa, "Fundamental analysis for visible-light communication system using LED lights," *IEEE Transactions on Consumer Electronics*, vol. 50, no. 1, pp. 100–107, 2004.

[32] M. Aminikashani, W. Gu, and M. Kavehrad, "Indoor positioning with ofdm visible light communications," in *2016 13th IEEE annual consumer communications & networking conference (CCNC)*. IEEE, 2016, pp. 505–510.

[33] B. Lin, X. Tang, Z. Ghassemlooy, C. Lin, and Y. Li, "Experimental demonstration of an indoor vlc positioning system based on ofdma," *IEEE Photonics Journal*, vol. 9, no. 2, pp. 1–9, 2017.

[34] H. Yang, C. Chen, W.-D. Zhong, A. Alphones, S. Zhang, and P. Du, "Demonstration of a quasi-gapless integrated visible light communication and positioning system," *IEEE Photonics Technology Letters*, vol. 30, no. 23, pp. 2001–2004, 2018.

[35] H. Yang, C. Chen, W.-D. Zhong, S. Zhang, and P. Du, "An integrated indoor visible light communication and positioning system based on fbmc-scm," in *2017 IEEE Photonics Conference (IPC)*. IEEE, 2017, pp. 129–130.

[36] Salustri, https://github.com/trilusa/RetroRay, [Online].

[37] J. M. Kahn and J. R. Barry, "Wireless infrared communications," *Proceedings of the IEEE*, vol. 85, no. 2, pp. 265–298, 1997.

[38] H. Haas, M. S. Islim, C. Chen, and H. Abumarshoud, *An Introduction to Optical Wireless Mobile Communication*. Artech House, 2021.

[39] Thorlabs, https://www.thorlabs.com/newgrouppage9.cfm?objectgroup_id=285, [Online].

[40] ——, https://www.thorlabs.com/newgrouppage9.cfm?objectgroup_id=6973&tabname=N-BK7, [Online].

Authorized licensed use limited to: UNIVERSITY OF NEW MEXICO. Downloaded on June 04,2023 at 15:25:36 UTC from IEEE Xplore. Restrictions apply.
© 2023 IEEE. Personal use is permitted, but republication/redistribution requires IEEE permission. See https://www.ieee.org/publications/rights/index.html for more information.